AGU PUBLICATIONS

JGR

Journal of Geophysical Research: Space Physics

RESEARCH ARTICLE
10.1002/2016JA022995

Key Points:
- ULF waves simultaneously interact with different ion species
- The resonant oxygen ions and protons show different behaviors in pitch angle and phase space density
- An approach to diagnose the fundamental-mode electric field morphology using the resonant ion signals

Correspondence to:
Q. G. Zong,
qgzong@gmail.com

Citation:
Ren, J., Q. G. Zong, X. Z. Zhou, R. Rankin, and Y. F. Wang (2016), Interaction of ULF waves with different ion species: Pitch angle and phase space density implications, *J. Geophys. Res. Space Physics*, *121*, 9459–9472, doi:10.1002/2016JA022995.

Received 24 MAY 2016
Accepted 14 SEP 2016
Accepted article online 17 SEP 2016
Published online 8 OCT 2016

Interaction of ULF waves with different ion species: Pitch angle and phase space density implications

Jie Ren[1], Q. G. Zong[1], X. Z. Zhou[1], R. Rankin[2], and Y. F. Wang[1]

[1]Institute of Space Physics and Applied Technology, Peking University, Beijing, China, [2]Department of Physics, University of Alberta, Edmonton, Alberta, Canada

Abstract ULF waves can accelerate/decelerate the charged particles including the ring current ions via drift-bounce resonance, which play an important role in the dynamics of ring current during storm times. This study compares the different behaviors of oxygen ions (10.5–35.1 keV) and protons (0.3–12.3 keV) which simultaneously interact with Pc5 ULF waves observed by Cluster on 3 June 2003. The ULF waves are identified as the fundamental mode oscillations. Both oxygen ions and protons show periodic energy dispersion and pitch angle dispersion signatures, which satisfy the drift-bounce resonance condition of N=2. The different behaviors of oxygen ions and protons include (1) the resonant energy of oxygen ions is higher than that of protons due to mass difference; (2) the phase space density (PSD) of oxygen ions show relative variations (3.6–6.3) that are much larger than that of protons (<0.4), which indicates a more efficient energy exchange between oxygen ions and ULF waves; (3) the PSD spectra show that oxygen ions are accelerated, while protons are decelerated, which depend on the radial gradient of their PSD; (4) the pitch angle distributions (PADs) of the oxygen ions and protons show negative slope and bidirectional field-aligned features, respectively, which is related to the preexisting state of ion PADs before the interaction with the ULF waves. In addition, the resonant ions with peak fluxes tracing back to the magnetic equator are always collocated with the accelerating (westward) electric field, which indicate that the ions are mainly accelerated near the magnetic equator and the electric field intensity of ULF waves peaks there.

1. Introduction

Ultralow frequency (ULF) waves play an important role in mass, momentum, and energy transport processes within the magnetosphere [e.g., *Takahashi et al.*, 2006; *Zong et al.*, 2008]. Most of Pc5 ULF waves with the period of 150–600 s [*Jacobs et al.*, 1964] are thought to be generated by solar wind sources [*Fujita et al.*, 2011]. As shown in Figure 1a, Pc5 ULF waves can be excited through a variety of mechanisms, including Kelvin-Helmholtz instability in the magnetopause[*Chen and Hasegawa*, 1974; *Rae et al.*, 2005; *Fujita et al.*, 1996; *Lavraud et al.*, 2011], impulsive compression arising from sudden enhancement of solar wind dynamic pressure [*Zong et al.*, 2007, 2012; *Yang et al.*, 2010], and direct penetration of solar wind variations into the magnetosphere [*Kepko et al.*, 2002; *Kepko and Spence*, 2003]. Kelvin-Helmholtz surface waves or fast magnetosonic waves excited at the magnetopause can couple to local Alfvén waves and excite ULF waves through field line resonance in the inner magnetosphere [*Hughes*, 1994; *Rae et al.*, 2005; *Zong et al.*, 2012; *Kepko and Spence*, 2003].

These excited ULF waves would further interact with charged particles. *Southwood and Kivelson* [1981, 1982] developed a theory of charged particle behavior within poloidal-mode ULF waves with azimuthal electric field oscillations. The drift-bounce resonant condition between charged particles and poloidal-mode ULF waves can be described theoretically as [*Southwood et al.*, 1969]

$$\omega - m\omega_d = N\omega_b \tag{1}$$

where ω and m are the wave angular frequency and azimuthal wave number, ω_d and ω_b are the particle drift and bounce angular frequencies, respectively, and N is an integer which depends on the wave harmonic modes. As shown in Figure 1b, charged particles can be accelerated by the fundamental poloidal-mode standing ULF waves via drift resonance (red line, $N=0$) and drift-bounce resonance (blue line, $N=2$) [*Southwood and Kivelson*, 1981, 1982]. *Elkington et al.* [1999] proposed that there could be drift-bounce resonance for

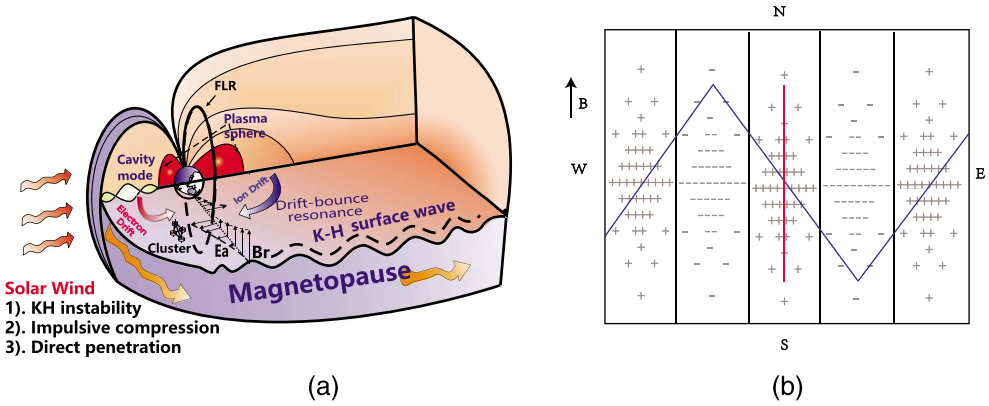

Figure 1. Schematics of solar wind exciting ULF waves (based on *Zong et al.* [2008]) and wave-particle resonant interactions in a fundamental mode of a standing poloidal Alfvén waves (based on *Southwood and Kivelson* [1982]). (a) The solar wind excites Kelvin-Helmholtz surface waves or fast magnetosonic waves at the magnetopause and then causes field line resonances. Standing waves and wave-particle resonant interactions can be observed by Cluster fleet. (b) The plus and minus symbols represent accelerated and decelerated electric field, respectively. The red line indicates the guiding center trajectory of particles than satisfies the drift resonant condition, and the blue line represents the guiding center trajectory of particles that satisfies the drift-bounce resonant condition of $N=2$.

toroidal-mode ULF waves when the noon–midnight asymmetry of the geomagnetic field is produced by the impact of the solar wind.

Many observational studies have revealed that ULF waves can significantly impact the dynamics of radiation belt energetic electrons and ring current ions in the inner magnetosphere [e.g., *Zong et al.*, 2009; *Rostoker et al.*, 1998; *Zong et al.*, 2012; *Yang et al.*, 2011b]. Observations of drift resonance between ULF waves and radiation belt electrons have been published extensively. *Zong et al.* [2009] observed that interplanetary shocks and/or solar wind pressure pulses with small dynamic pressure change have a significant impact on the radiation belt dynamics. *Dai et al.* [2013] unambiguously identified the wave mode and the phase relation between electric fields and particle fluxes, providing direct evidence of drift resonance with the fundamental mode poloidal waves. *Claudepierre et al.* [2013] reported the Van Allen Probes observations of localized drift resonance between poloidal-mode ULF waves and 60 keV electrons. When drift resonance occurs in a specific energy band, there will be phase shift of particle fluxes around the resonant energy [*Dai et al.*, 2013; *Zhou et al.*, 2015], and the peak-to-valley ratio of the flux oscillation at this energy will be maximum compared to the adjacent energies in some cases [*Yang et al.*, 2010; *Claudepierre et al.*, 2013]. The drift-resonance theory has also been applied to understand the growth and damping of ULF waves by introducing a time-dependent imaginary wave frequency [*Zhou et al.*, 2015, 2016]. A number of authors have suggested a link between ULF waves and MeV electron acceleration [e.g., *Mathie and Mann*, 2000; *Rostoker et al.*, 1998]. *Foster et al.* [2015] proposed that prompt acceleration caused by impulsive shock-induced electric fields and subsequent ULF waves comprise a significant mechanism for the relativistic electron acceleration in the outer radiation belt.

The interaction between energetic ions (H^+, O^+) and ULF waves in the ring current region has also attracted a lot of research interest [e.g., *Zong et al.*, 2012; *Yang et al.*, 2011a, 2011b; *Dai et al.*, 2013; *Ren et al.*, 2015]. *Zong et al.* [2012] observed multiple energy dispersion signatures of ions associated with ULF waves and inferred that the ring current ions (H^+, O^+) can be accelerated by poloidal-mode ULF waves excited by interplanetary shock impact. *Yang et al.* [2011a] reported that during storm time, ring current O^+ ions may be accelerated or decelerated by fundamental poloidal-mode ULF waves via drift-bounce resonance. *Ren et al.* [2015] reported that Cluster observed the third harmonic mode ULF waves that can simultaneously interact with both substorm-injected "hot" particles and cold outflow ions. Based on the different pitch angle distributions (PADs) associated with different standing wave harmonics, the ion PADs data can be used to diagnose the harmonic mode of ULF standing waves [*Takahashi et al.*, 1990; *Yang et al.*, 2011b; *Ren et al.*, 2015].

Ions (H^+, O^+, etc.) with tens to hundreds of keV are thought to be the main carriers of the ring current energy [e.g., *Williams*, 1981, 1983, 1985]. The bulk (~90%) of the ring current is in the energy range of 15–250 keV [*Williams*, 1981]. Observations show that H^+ ions are the dominant ring current ion species during quiet times, while O^+ ions become dominant during geomagnetic activities [e.g., *Zong et al.*, 2001; *Daglis et al.*, 1999;

Fu et al., 2001]. According to quantitative calculations based on equation (1), *Zong et al.* [2012] proposed that as for ions in the energy range from 10 to 500 keV, oxygen ions can more easily satisfy the drift-bounce resonant condition for $N = 0, \pm 1, \pm 2$. Therefore, understanding of the different behaviors of H^+ and O^+ interacting with ULF waves will lead to improve the understanding of the roles of ULF waves in the dynamics of ring current during storm times.

Although significant progress has been made, it remains a challenge to quantify the impact of ULF waves on energetic particle dynamics, since the global distributions of the electric field and charged particles are not clear yet. Therefore, it is important to study the morphology of electric field as a function of magnetic latitude. By solving the uncoupled standing Alfvén wave equations with prescribed background magnetic field, plasma density distribution and ionosphere boundary condition, an MHD analysis could determine the global distribution, frequency, and phase relationship of the electric field and magnetic field oscillations [*Cummings et al.*, 1969; *Takahashi et al.*, 2011; *Degeling et al.*, 2008; *Dai et al.*, 2013]. These authors have solved the ideal MHD field line eigenmode equations with an assumed model for the magnetic field (typically a dipole field) and density as a function of magnetic latitude. The profile of the wave electric field varies under different ionosphere boundary. Their results show that the intensity of the fundamental mode electric field either remains uniform up to a high magnetic latitude, or peaks at high magnitude latitude (rather than at the equator). However, the schematic of the fundamental-mode electric field in some previous study [e.g., *Southwood and Kivelson*, 1982; *Yang et al.*, 2011b] shows that the intensity peaks at the magnetic equator so that particles in resonance can be accelerated or decelerated over many bounces. In this study, we proposed an approach to diagnose the morphology of the electric field as a function of magnetic latitude using the resonant ion signals.

On 3 June 2003, Cluster observed the simultaneous interaction between Pc5 ULF waves and different kinds of ions including H^+ and O^+. The main objective of this paper is to show the different behaviors of these ions while interacting with ULF waves and further to provide an approach to diagnose the electric field morphology of ULF waves via the signals of resonant ions. Sections 2 and 3 show the data sources and observations, respectively. Discussions are presented in section 4. Finally, the conclusions are given in section 5.

2. Data Sources

Satellite data in this study are mainly from Cluster constellation [*Escoubet et al.*, 2001], which operates on a polar elliptical orbit of $4 \times 19.6\ R_E$. The PADs and spectrogram of ions are measured by the Cluster Ion Spectrometry experiment (CIS), which consists of a Hot Ion Analyzer (HIA) and a time-of-flight ion COmposition and DIstribution Function analyzer (CODIF) [*Rème et al.*, 2001]. HIA instrument is capable of detecting a full three-dimensional distribution of ions in the energy range from 5 eV/e to 32 keV/e without distinguishing the species. CODIF instrument provides the three-dimensional measurements of the major ions (H^+, He^+, He^{++}, and O^+) in the energy range ~25 eV/e–40 keV/e. The energetic electron fluxes measured by Cluster are from the Research with Adaptive Particle Imaging Detectors (RAPID) measurement [*Wilken et al.*, 1997]. The Fluxgate Magnetometer (FGM) [*Balogh et al.*, 1997] and the HIA instrument provide the magnetic field data and ions velocity data to calculate the electric field through the equation $\mathbf{E} = -\mathbf{V} \times \mathbf{B}$ [*Zong et al.*, 2007]. The Cluster data are available at the Cluster Science Archive[*Laakso et al.*, 2010].

The energetic electron data at the geosynchronous orbit are measured by Synchronous Orbit Particle Analyzer (SOPA) detectors on board Los Alamos National Laboratory (LANL) spacecrafts, which have the detecting energy range from 50 keV to approximately 26 MeV. In addition, the solar wind observations are from the Wind spacecraft [*Ogilvie et al.*, 1995], and geomagnetic indices (*SYM-H* and *AL*) are from the OMNI data.

3. Observation

On 3 June 2003, between 2150 and 2230 UT, Cluster C1 was traveling inbound from the duskside magnetosphere (at ~1600 magnetic local time (MLT), Figure 2a) toward the inner magnetosphere from the Southern to Northern Hemisphere (Figure 2b). The magnetic field configuration in Figure 2b is calculated from the Tsyganenko T89 model [*Tsyganenko*, 1989] with $Kp = 3$.

Figures 3a and 3b show the spin-averaged energetic electron data in the energy channel of 105–150 keV from 1991-080 and 1990-095 satellites, respectively. Periodic modulations of the electron fluxes were first observed by C1 at about 2204 UT and coincide with the appearance of Pc5 ULF waves labeled by the red vertical dashed line. In Figure 3c, the amplitude of the total magnetic field observed by Cluster C1 also shows periodic

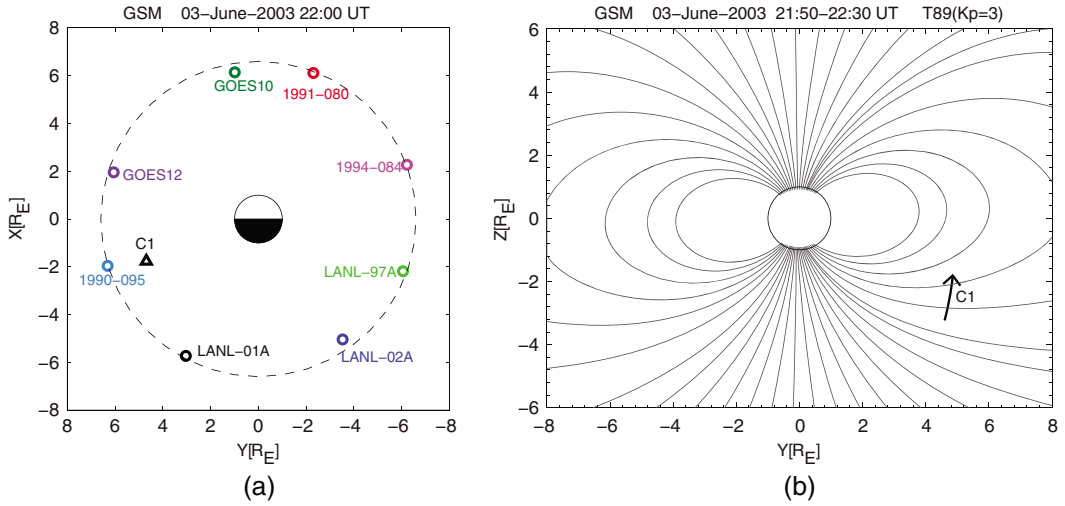

Figure 2. Spacecraft positions in the GSM coordinate system: (a) locations in the *X-Y* plane at 2200 UT on 3 June 2003; (b)magnetic field configuration in the *Y-Z* plane obtained by the Tsyganenko T89 model and the spacecraft trajectory of Cluster C1 from 2150 UT to 2230 UT.

modulations that were also observed by the LANL satellites during the same time interval. The solar wind velocity data in Figure 3d is shifted by 31 min to account for the solar wind propagating time, according to the distance of the Wind spacecraft (243 R_E) and the average upstream flow velocity (830 km/s). The *SYM-H* index in Figure 3e increased corresponding to the enhancement of solar wind velocity impacting on the magnetopause. The *AL* index in Figure 3f shows that this event occurred during the recovery phase of a large substorm.

3.1. Overview of Energetic Ion Behaviors and Associated ULF Waves

Figure 4a shows the observational overview of ions (mostly protons) from the HIA instrument and oxygen ions from the CODIF instrument. The oxygen ion fluxes from the CODIF instrument are about one magnitude lower than those from the HIA instrument in the same energy range, but with different PADs, which confirms that protons are the dominant ion species detected by HIA. The first four rows of Figure 4a show proton energy spectrograms and PADs in three representative energy channels, respectively. The PADs in the energy channel of 16.3 keV and 28.9 keV show modulations that are independent of the pitch angle. Bidirectional field-aligned features appear at 3.9 keV with the modulations much more remarkable in the parallel and antiparallel directions. The last four rows in Figure 4a show the O^+ energy spectrogram and PADs in three representative energy channels, respectively. Pitch angle dispersion signatures are observed in the energy channel of 17.0 keV and 27.6 keV, but not at 4.0 keV.

To better study the ULF wave properties, both the magnetic and electric fields are projected into a local mean-field-aligned (MFA) coordinate system [*Takahashi et al.*, 1990; *Zong et al.*, 2012]. Different mode magnetic and electric fields are shown in Figure 4b. The poloidal (toroidal) mode consists of the radial (azimuthal) magnetic field component and azimuthal (radial) electric field component. As shown in the bottom row of Figure 4b, the phase differences between electric field and magnetic field oscillations for both poloidal (blue line) and toroidal mode (red line) are close to 90° in the frequency of 4.2 mHz, which suggest that they are standing waves along the magnetic field. For the poloidal mode, E_a leads B_r by 90° in the Southern Hemisphere, which indicates that this standing wave is an odd harmonic mode (e.g., fundamental mode and third harmonic mode) [*Singer et al.*, 1982].

3.2. Drift Resonance of the Energetic Electrons

We next study the energetic electron flux modulation observed by Cluster C1/RAPID during 2215–2230 UT, which is marked by the shadow area in Figure 5a. The first and second rows in Figure 5a show the original and residual fluxes of the energetic electrons in different energy channels, respectively. Residual flux is defined as $\frac{J-J_0}{J_0}$, where J is the original flux and J_0 is a 15 min, running boxcar average of J. Note that the normalized flux modulation is strongest at 94.5 keV and weaker at energies above and below this energy channel, which is also demonstrated by the relevant peak-to-valley ratio of the flux oscillations in the bottom row of Figure 5a. The first and second rows in Figure 5b show the original and residual fluxes of the energetic electrons in different

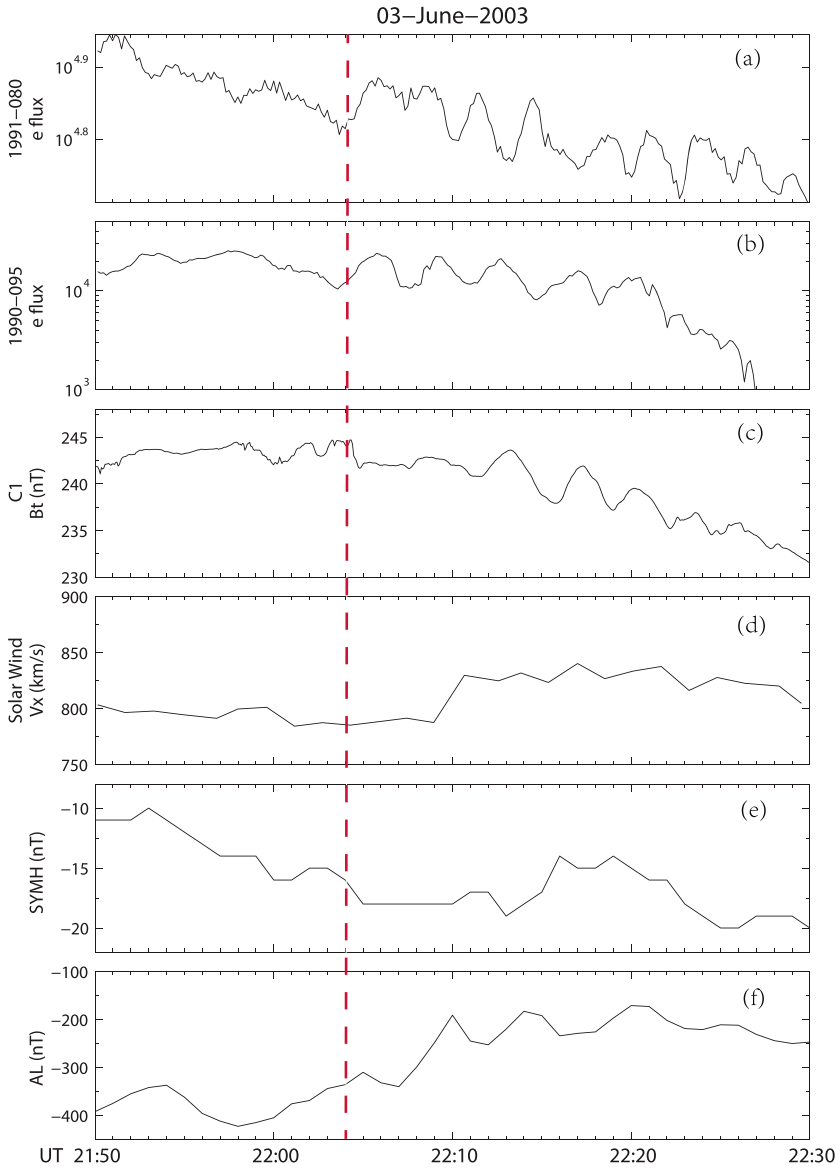

Figure 3. (a and b) Spin-averaged energetic electron data in the energy channel of 105–150 keV from 1991-080 and 1990-095, respectively. (c) Magnetic field magnitudes from Cluster C1. (d) V_x component of the solar wind velocity. (e) *SYM-H* index. (f) *AL* index. The red vertical dashed line indicates the onset time of the oscillations of the electron flux observed by LANL spacecrafts.

energy channels from 1990-095/SOPA, respectively. The strongest modulation of electron fluxes appears in the energy channel of 105–150 keV. These results imply a drift-resonance interaction between the energetic electrons and fundamental poloidal-mode ULF waves with a resonant energy of about 100 keV. Both the original data and wavelet analyses (not shown here) show that there are clear phase shift of the electron fluxes from 1990-095 and 1991-080, which can be resulted by the drift resonance between the electron flux and fundamental mode ULF waves. When passing through different *L* value regions, Cluster C1 observed unstable phase differences of electron flux. This phenomena were once observed in the previous work studying drift resonance between ULF waves and electron flux from Cluster/RAPID [e.g., *Yang et al.*, 2010; *Zong et al.*, 2007].

The bounce frequency of a 100 keV electron in the inner magnetosphere is much higher than the drift frequency and the Pc5 wave frequency. Based on equation (1), the drift-bounce resonance for energetic electrons could only be excited with $N=0$. Then equation (1) is equivalent to the drift resonance condition: $\omega - m\omega_d = 0$. We estimate the drift frequency of a 100 keV, 90° pitch-angle electron drifting at $L=7$ in a dipole field to be

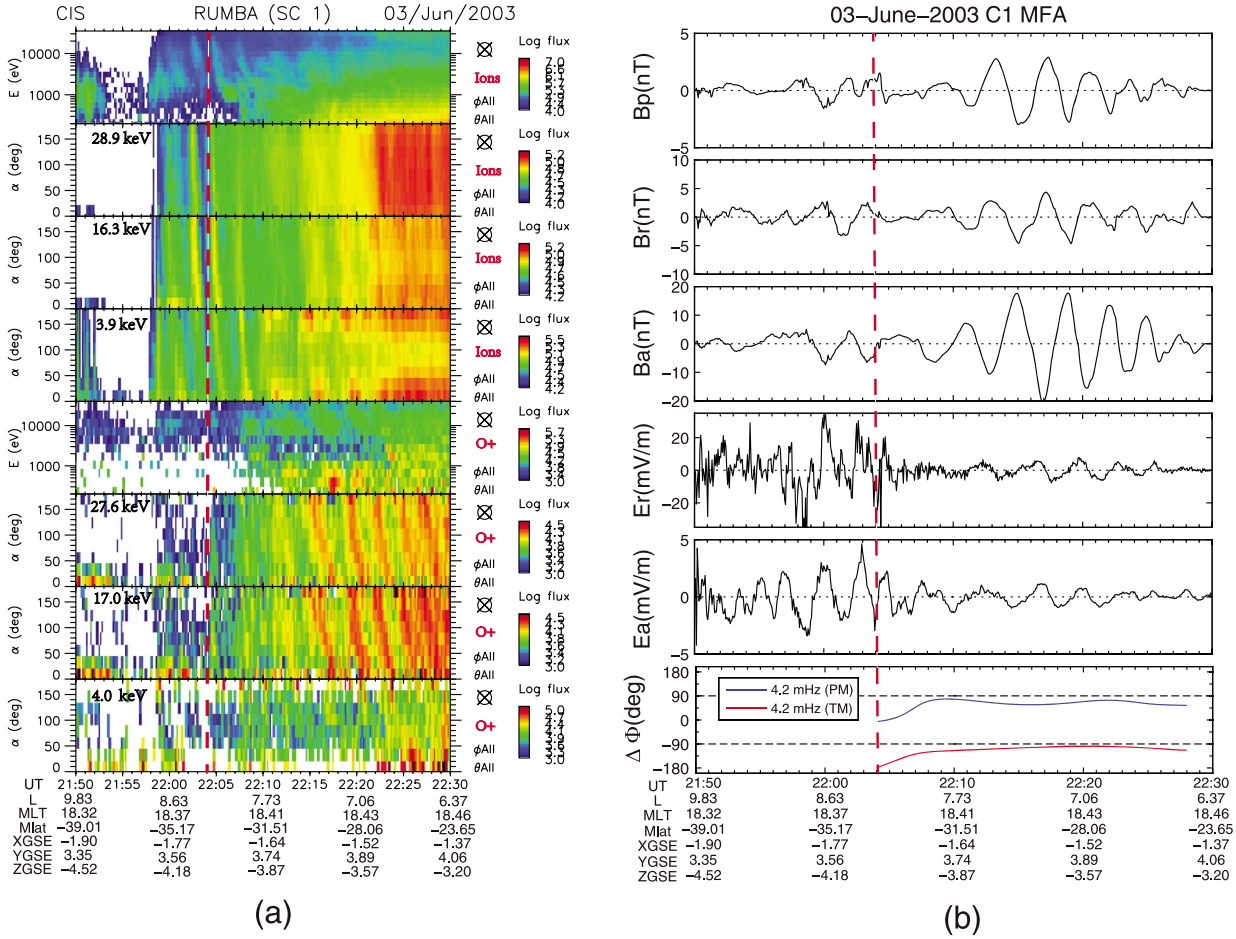

Figure 4. (a) Observation of ions by C1/HIA and observation of O+ by C1/CODIF: the first four rows are ions energy spectrum, representative PADs of ions in energy channels of 28.9 keV, 16.3 keV, and 3.9 keV, respectively; the last four rows are O+ energy spectrogram, representative PADs of O+ in energy channels of 27.6 keV, 17.0 keV, and 4.0 keV, respectively. (b) The magnetic and electric fields are projected into the local mean field-aligned (MFA) coordinate system. From top to bottom are B_P, B_r, B_a, E_r, E_a, and cross phase between electric and magnetic fields for poloidal-mode (blue line) and toroidal mode (red line) at the frequency of 4.2 mHz, respectively. The red vertical dashed line indicates the onset time of the oscillations of the electron flux observed by LANL spacecrafts.

0.35 mHz. Using this value and the observed wave frequency (4.2 mHz), the drift-resonance condition predicts an azimuthal wave number of $m = 12$.

3.3. Drift-Bounce Resonant Ions and Relationship to Poloidal-Mode Electric Field

In order to study the relationship between drift-bounce resonant ions and the poloidal-mode electric field, the PADs of the oxygen ions (8.3–35.1 keV) and protons (0.3–12.3 keV) from high- to low-energy channels are shown in Figures 6a and 6b, respectively. The pitch angle dispersion signatures of oxygen ions are very clear in the energy range from 10.5 keV to 35.1 keV, and they become indistinct at energies lower than 10.5 keV. In contrast, the PADs of protons show bidirectional field-aligned features.

A natural speculation on the pitch angle dispersion signature in Figure 6 is that the peaks of ion fluxes all result from an ion acceleration process, which mainly occurs near the magnetic equator if the intensity of the fundamental mode electric field peaks there. In this scenario, the dispersion should arise from the different time delay due to the ions (with different energies/pitch angles) traveling from the equator to the spacecraft location. The time difference of a bouncing ion with an certain equatorial pitch angle α_{eq} moving from one point to another point along the same magnetic field line is described as [*Hamlin et al.*, 1961]

$$\delta t = \frac{LR_E}{\sqrt{2W/m_p}} \int_{\lambda_1}^{\lambda_2} \cos\lambda \left(1+3\sin^2\lambda\right)^{1/2} \left[1-\sin^2\alpha_{eq}\frac{\left(1+3\sin^2\lambda\right)^{1/2}}{\cos^6\lambda}\right]^{-1/2} \mathrm{d}\lambda \quad (2)$$

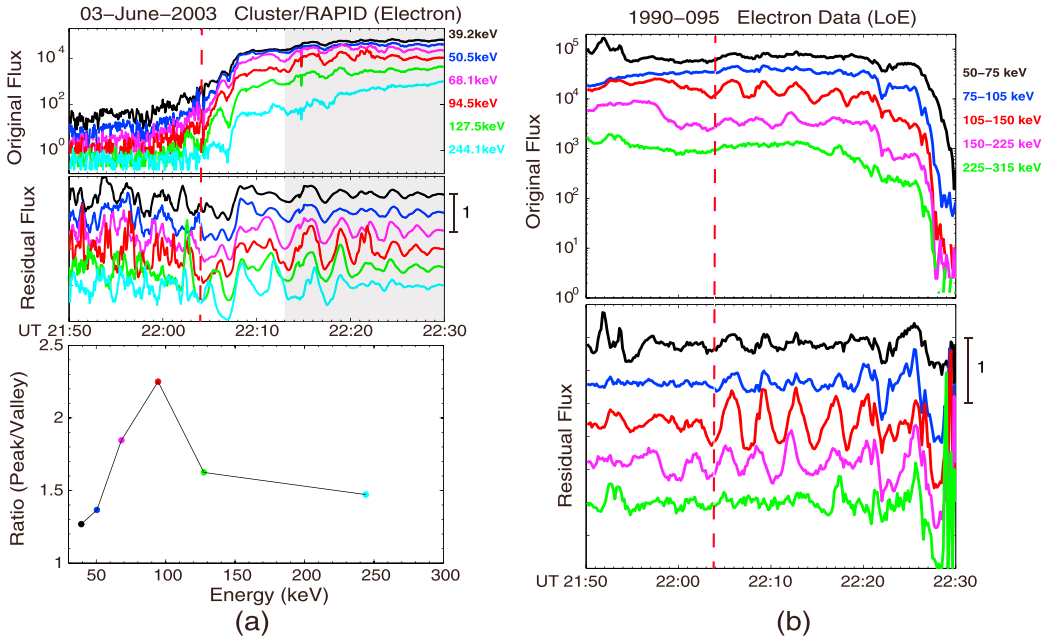

Figure 5. Electron observation by Cluster C1/RAPID and 1990-095/SOPA: (a) from top to bottom are original electron flux, residual electron flux ($\frac{J-J_0}{J_0}$), and peak-to-valley ratio of each energy channel from Cluster C1/RAPID; (b) from top to bottom are original electron flux and residual electron flux ($\frac{J-J_0}{J_0}$) from 1990-095/SOPA.

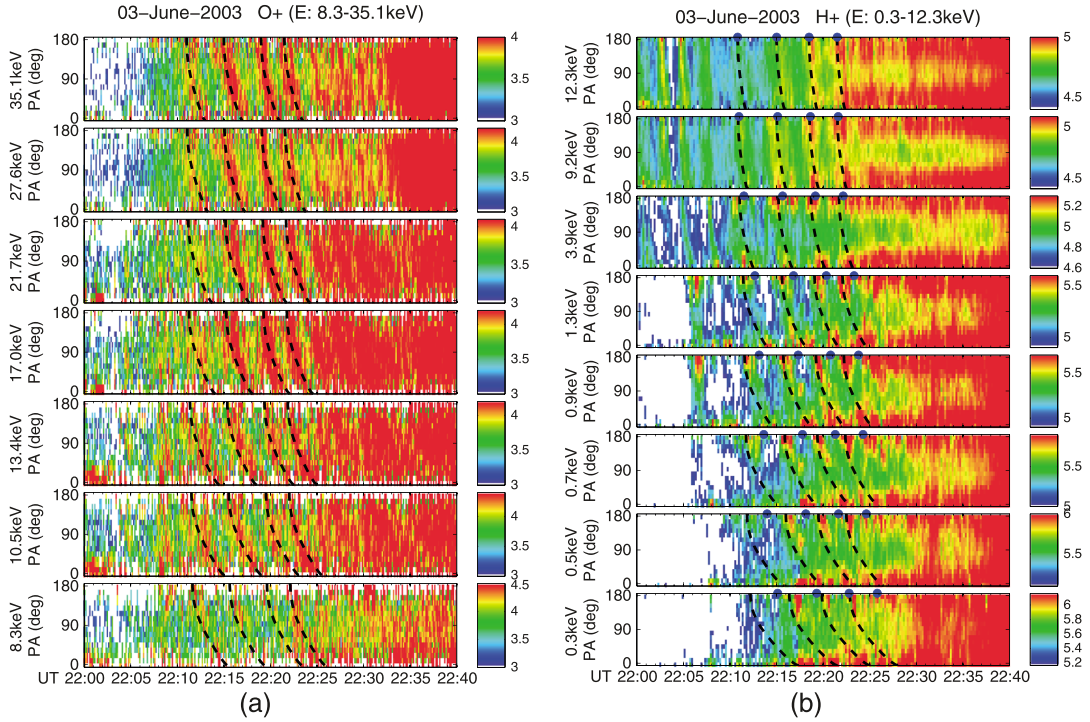

Figure 6. (a) PADs of the oxygen ions in different energy channels as measured by the CODIF instrument from C1; the black dashed lines in each channel indicate the calculated pitch angle dispersion signatures of the oxygen ions with the maximum flux, which originate from the magnetic equator. (b) PADs of the ions (mainly protons) in different energy channels as measured by the HIA instrument from C1. The black dashed lines in each channel indicate the calculated pitch angle dispersion signatures of the protons with the maximum flux, which originate from the magnetic equator; the blue dots indicate the arrival time of the protons in the antiparallel direction with the maximum flux, which come from the ionosphere at the Northern Hemisphere.

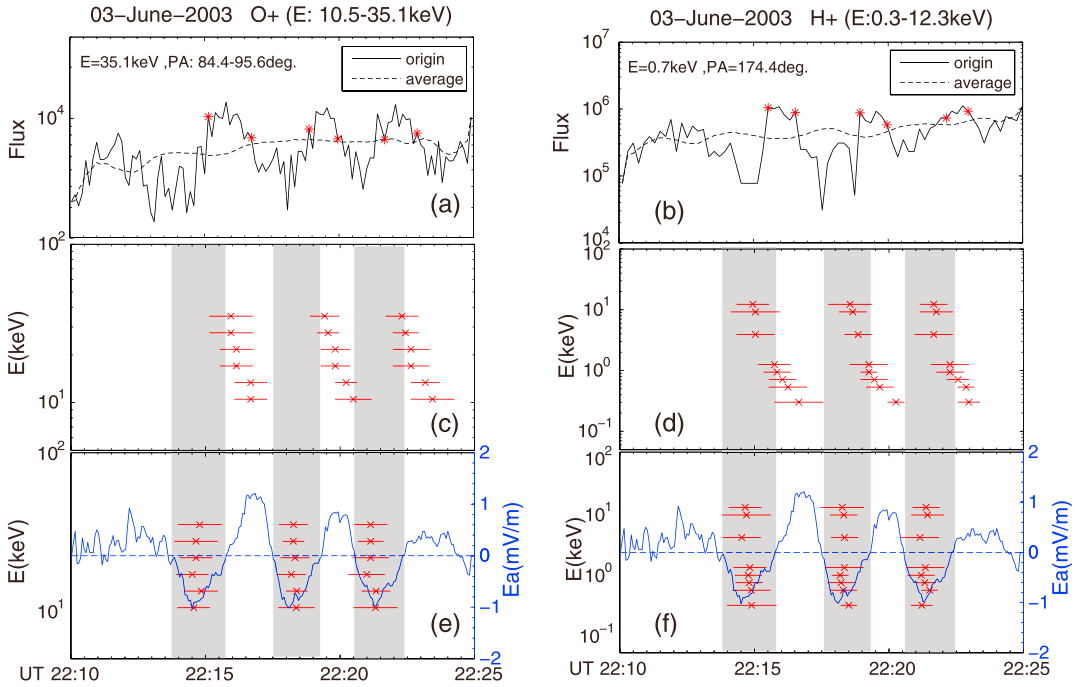

Figure 7. (a) Solid line is the original flux (*J*) of 35.1 keV O+ at the pitch angle from 84.4° to 95.6° ; dashed line is a 15 min, running boxcar average of the original; the red stars mark the start and end points of the original flux higher than the average. (b) The same as Figure 7a but for 0.7 keV, 174.4° protons. (c) The red segments indicate the duration of the original flux higher than the average in the energy range from 10.5 to 35.1 keV with the pitch angle from 84.4° to 95.6°. (d) The same as Figure 7c but for protons in the energy range from 0.3 to 12.3 keV with the pitch angle of 174.4°. (e) The red segments are those in Figure 7c after traced back to the magnetic equator; the blue line is the poloidal-mode electric field (E_a). (f) The same as Figure 7e but for protons.

where L is the L shell parameter, R_E is Earth's radius, W is the particle energy, m_p is the particle mass, λ is the magnetic latitude, and α_{eq} is the equatorial pitch angle. The peaks of the oxygen (35.1 keV) and proton (12.3 keV) flux at 180° are traced track to the magnetic equator based on equation (2). Their observed time at the magnetic equator are regarded as the reference points, and then we calculate the observed time of the peaks (with different energies/pitch angles) at the spacecraft location based on the equation (2). The results are represented by the dashed lines in Figures 6a and 6b and are consistent with the observations. If we assume that the protons in the antiparallel direction are mainly accelerated during the upgoing path from the northern ionosphere, the arrival time of these protons, marked by the blue dots in Figure 6b, is clearly inconsistent with the observations.

In order to further explore the relationship between the accelerated ions and the electric field of the fundamental poloidal-mode ULF waves, the accelerated oxygen ions (10.5–35.1 keV) and protons (0.3–12.3 keV) are traced back to the magnetic equator (see Figures 7a and 7b). The solid lines are the original flux of 35.5 keV oxygen ions in the pitch-angle range from 84.4°to 95.6°and 0.7 keV protons at the pitch angle of 174.4°, respectively; the dashed lines are a 15 min, running boxcar average of the original flux. The red stars mark the start and end points of the original flux higher than the average. The duration of the original flux higher than the average in other energy channels can be extracted in the same way and is indicated by the red segments in Figures 7c and 7d. These red segments are then traced back to the magnetic equator (see Figures 7a and 7b), show no energy dispersion, and are approximately collocated with the shaded intervals, indicating that the westward electric field has accelerated these ions near the magnetic equator.

The wavelet analysis in Figure 8 shows that the oscillations of O^+ flux, proton flux and poloidal-mode ULF waves are in the same range of periods. As shown in Figures 8b and 8d, the wave bandwidth defined by the wave power dropping to half its maximum strength (red line) is indicated by the blue lines. Figure 8f shows the calculated frequency of the fundamental poloidal mode in the dipole magnetic field [*Degeling et al.*, 2010]. In calculation, we adopt the perfect ionospheric conductivity, the power law density model with the power index

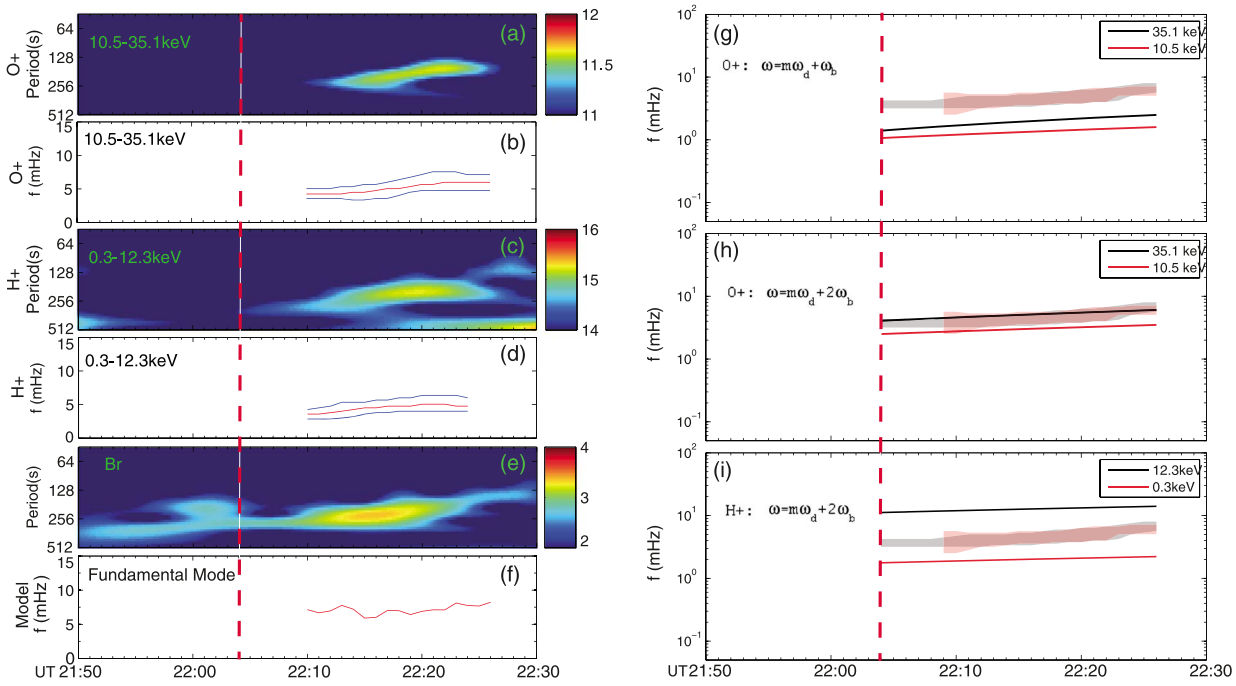

Figure 8. (a) Wavelet spectrum of oxygen ions (10.5–35.1 keV). (b) The blue lines indicate the edges of the wave bandwidth as where the wave power in Figure 8a decreases to half of its maximum strength (red line). (c) Wavelet spectrum of protons (0.3–12.3 keV). (d) The blue lines indicate the edges of the wave bandwidth as where the wave power in Figure 8c decreases to half of its maximum strength (red line). (e) Wavelet spectrum of B_r component of poloidal mode. (f) Theoretical eigenfrequency of the fundamental poloidal mode. (g) The red and black lines indicate the sum of $m\omega_d$ and ω_b for O+ in 10.5 keV and 35.1 keV, respectively. The gray and red shadow areas indicate the wave bandwidth of B_r and E_a as where the wave power decreases to half of their maximum strength, respectively. (h) The red and black lines indicate the sum of $m\omega_d$ and $2\omega_b$ for O+ at 10.5 keV and 35.1 keV, respectively. (i) The red and black lines indicate the sum of $m\omega_d$ and $2\omega_b$ for protons at 0.3 keV and 12.3 keV, respectively.

of 4.0 [*Cummings et al.*, 1969], equatorial number density derived from spacecraft potential [*Pedersen et al.*, 2008; *Liu et al.*, 2013], and assumed that the particle are all protons. The calculated frequency is higher than the observed frequency indicated by the red lines in Figure 8b and 8d. The observations from Cluster/CIS shows that the O^+ ion density is about one tenth of the proton density. When the O^+ ions are taken into accounted, the calculated frequency will be lower and consistent with the observed frequency, which indicates that the observed ULF waves are the fundamental mode. In Figures 8h–8j, the wave bandwidth of B_r and E_a are marked by the gray and red shadow areas, respectively. For oxygen ions in the energy range from 10.5 to 35.1 keV, the sum of drift frequency and twice the bounce frequency exactly coincides with the wave bandwidth, which satisfies the drift-bounce resonance condition ($N = 2$) between ions and fundamental poloidal-mode ULF waves. For protons in the energy range from 0.3 to 12.3 keV, the sum of drift frequency and twice the bounce frequency overlaps with the wave bandwidth although its range is much wider.

4. Discussion

As shown in Figure 3, the Pc5 ULF waves in this study were excited following the enhancement of the high-speed solar wind impacting on the magnetosphere, which probably account for the ULF wave generation. Most of Pc5 ULF waves are regarded to be generated by solar wind sources [*Fujita et al.*, 2011; *Mathie and Mann*, 2001]. During storm and substorm activities, the enhanced energetic particles also could provide free energy for the ULF waves through drift-bounce resonance [e.g., *Chen and Hasegawa*, 1991; *Cheng and Qian*, 1994; *Southwood*, 1976; *Dai et al.*, 2013]. In this study, these observed ULF waves are identified as the fundamental mode according to the resonance between ULF waves and different energetic particles, phase difference between B_r and E_a, and modeling calculation. In addition, both GOES 10 and GOES 12, located between 1991-080 and 1990-095, did not observe any obvious magnetic field oscillations at the equator, which also indicates that these ULF waves are the fundamental mode with a node at the equator.

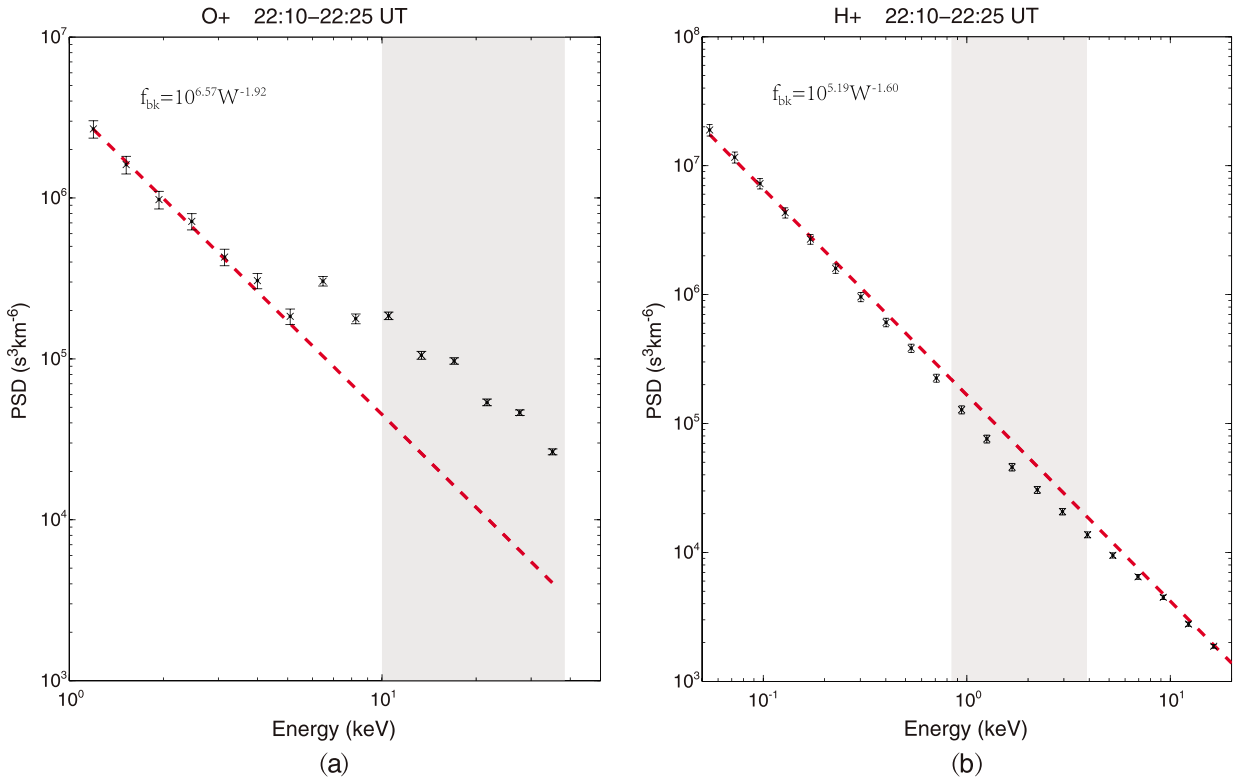

Figure 9. The averaged phase space density spectra of (a) oxygen ions and (b) protons over the time periods from 2210 UT to 2225 UT. The dashed red lines indicate the power law fit of the spectra. The gray shadow areas in Figures 9a and 9b represent the energy range of oxygen ions (10.5–35.1 keV) and protons (0.85–4 keV), respectively.

4.1. Drift-Bounce Resonance of Ions and Related Energy Exchange

To examine the acceleration/deceleration process for oxygen ions (10.5–35.1 keV) and protons (0.3–12.3 keV), Figures 9a and 9b present the averaged phase space density (PSD) of oxygen ions (1–40 keV) and protons (0.05–20 keV) between 2210 and 2225 UT, respectively. The vertical error bars denote the standard deviations of PSD, which is estimated by $\sqrt{N_c}/N_c$, where N_c is the particle counts. The red dashed lines show the typical background spectra with a power law distribution($f_{bk}=f_0W^{-\gamma}$). Figure 9a shows that the accelerating process mainly occurs in the energy range (gray shadow area) of oxygen ions that satisfy the drift-bounce resonance condition for ULF waves that have frequencies in the observed range of the wave bandwidth (in Figure 8h). Based on the drift-bounce resonance condition, it is estimated that the energy range of protons satisfying the drift-bounce resonance in the wave bandwidth is about 0.85–4 keV (gray shadow area in Figure 9b) where the decelerating process mainly occurs. Therefore, ULF waves with frequencies within the bandwidth play the dominant role in the acceleration/deceleration of the resonant ions.

The spectra comparisons in Figure 9 suggest that the resonant oxygen ions and protons are accelerated and decelerated, respectively. The relative PSD variations of oxygen ions and protons in the gray shadow regions in Figure 9 are in the range of about 3.6–6.3 and 0.25–0.37, respectively. The relative PSD variations of oxygen ions are much larger than that of protons, which indicates more efficient energy exchange between oxygen ions and ULF waves.

During drift-bounce resonance, the first adiabatic invariant is conserved for the ions. In the westward (eastward) E_a, the drift-bounce resonant ions will be accelerated (decelerated) and move radially inward (outward). If there are much more ions close to the Earth than farther out ($\partial f/\partial L<0$), the ions will transport a net gain of energy to waves and their PSD will decrease [*McPherron*, 2005; *Dai et al.*, 2013]. Conversely, if there are much less ions close to the Earth than farther out ($\partial f/\partial L>0$), the ions will get a net gain of energy from waves, and their PSD will increase. The energy change of resonant particles interacting with the poloidal-mode ULF waves [*Zong et al.*, 2009, 2012] can be expressed as $dW/dt=q\vec{E}_a\cdot\vec{V}_d$, where dW/dt and $\vec{v}_d$ are the energy exchange rate and particle drift velocity, respectively. According to the drift-bounce resonant condition,

the resonant energy of oxygen ions is higher than that of protons due to mass difference, which results in higher energy exchange rate for oxygen ions.

Based on Liouville's theorem, the gyration-averaged change in f is given by $\delta f = -\delta W \frac{\partial f}{\partial W} - \delta L \frac{\partial f}{\partial L}$ [*Southwood and Kivelson*, 1981]. By taking $f_{bk} = f_0 W^{-\gamma}$, $\delta W = qV_d \delta E_a$ and $\delta L = \frac{m\delta W}{qB_e L\omega R_E^2} - \frac{irE_a}{B_e L\omega R_E^2}$, where B_e is the equatorial magnetic field on the field line and r is the local radial distance to the symmetry axis [*Southwood and Kivelson*, 1981], the relative PSD variations at a given time can be expressed as

$$\frac{\delta f}{f_{bk}} = \gamma q \delta E_a - \left(\frac{m\delta E_a V_d W^{\gamma}}{B_e L\omega R_E^2 f_0} - \frac{irE_a W^{\gamma}}{B_e L\omega R_E^2 f_0} \right) \frac{\partial f}{\partial L}. \quad (3)$$

The first term on the right side is independent of the resonant energy (W). But the second term on the right side has two parts that are proportional to $W^{\gamma+1}$ ($V_d \sim W$) and W^{γ}, respectively. The power law index (γ) for oxygen ions and protons are 1.92 and 1.60, respectively. Therefore, the second term accounts for the main difference of the relative PSD variations between oxygen ions and protons.

As shown in Figure 6, PADs of accelerated drift-bounce oxygen ions and protons show negative slope and bidirectional field-aligned features, respectively. The PADs of the accelerated drift-bounce oxygen ions in Figure 6a were reported in a previous study [*Yang et al.*, 2011a] and found to be a common phenomenon in the Southern and Northern Hemispheres [*Yang et al.*, 2011b]. The PADs of the accelerated drift-bounce resonant protons illustrated in Figure 6b have rarely rarely been reported or studied. *Chaston et al.* [2015] have suggested that ionospheric ions can be extracted from the ionosphere due to the action of broadband low-frequency kinetic Alfvén waves, which energize them from tens of eV to >50 keV as they move upward along geomagnetic field lines. This can result in the bidirectional field-aligned features in the ion PADs. In this study, the electric field and magnetic field observation from Cluster C1 also show evidence of broadband electromagnetic field fluctuations up to hundreds of hertz (not shown here), which may be correlated with the bidirectional field-aligned features of the proton PADs. *Malaspina et al.* [2015] proposed that broadband kinetic Alfvén waves which are modulated by ULF waves energize and modulate protons that travel outward along geomagnetic field lines. Figure 6b shows that the arrival time of the accelerated protons (blue dots) is not consistent with the observation if they are mainly energized during the upgoing process. The theoretical calculations encapsulated by equation (2), and the observations summarized by Figures 6b and 7b indicate that protons are directly modulated and energized by ULF waves via drift-bounce resonance wave-particle interactions. In summary, the bidirectional field-aligned features are formed via interactions with the broadband kinetic Alfvén waves or other processes, and the protons with this PAD will further interact with the ULF waves.

4.2. Relationship Between Resonant Ions and Electric Field Morphology

Figure 10 shows the schematics of three types of electric field morphology in magnetic latitude for fundamental poloidal-mode ULF waves. Also shown are the behaviors of accelerated ions satisfying the drift-bounce resonant condition of $N=2$ in the wave frame. Figure 10a shows the case with the electric field intensity maximized at the magnetic equator (an equator-concentrated case). Resonant ions moving along the blue line experience the strongest accelerating electric field (westward marked by plus signs) and the weakest decelerating electric field (eastward marked by minus signs) in each bounce period and thus get the largest net acceleration with maximum flux. The resonant ions observed by spacecraft, represented by the blue solid circle, can be traced back to the magnetic equator (the red solid cycle) based on equation (2). This location corresponds to the maximum accelerating electric field, which is further illustrated by the schematics at the bottom of Figure 10a. The ion flux tracing back to the magnetic equator is in antiphase with respect to the eastward electric field, which is consistent with the observation in Figures 7e and 7f. Figure 10b shows an alternative case with the electric field intensity maximized at the high magnetic latitude (equator-rarefied case). The resonant ions with maximum flux experience the largest accelerating electric field at the high magnetic latitude and the weakest electric field at the magnetic equator. As illustrated by the schematics at the bottom of Figure 10b, these ions flux after tracing back to the magnetic equator should be in phase with respect to the electric field. The latitude-uniform case in Figure 10c is that the electric field intensity is uniform up to high magnetic latitude along the magnetic field line. In one bounce period, ions experiences no net acceleration or deceleration. The ions with maximum flux should be observed when they experience the whole accelerating electric field, which is marked by the blue solid circle. At the satellite location, the ion flux should show energy

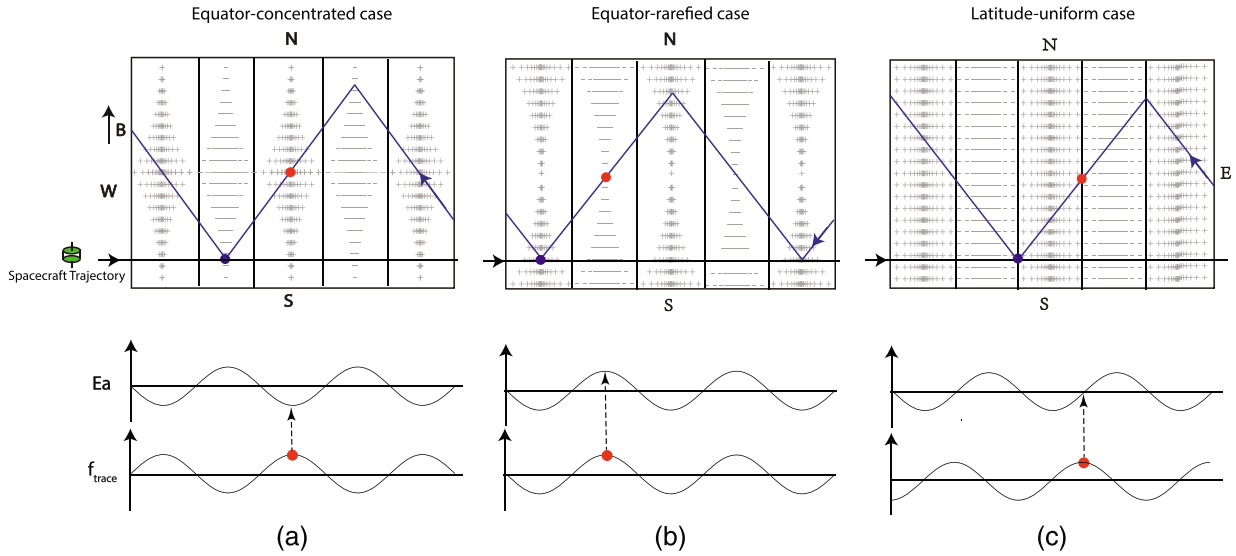

Figure 10. Schematics of wave-particle resonances in different cases of fundamental poloidal-mode electric field. (a) Equator-concentrated case: electric field intensity peaks at the magnetic equator. The plus and minus symbols represent accelerated and decelerated electric field, respectively. Electric field intensity corresponds to the density of symbols. The blue lines represent the guiding center orbits of the accelerated particles with the maximum flux. The black horizontal line indicates the spacecraft trajectory in wave frame. The blue and solid circles represent the positions where the maximum flux of accelerated particles is observed by spacecraft and should be observed after traced back to the magnetic equator. The schematics at the bottom show the phase relationship between electric field and ions flux after traced back to the magnetic equator. (b) Equator-rarefied case: intensity peaks in the high magnetic latitude and is lower at magnetic equator. (c) Latitude-uniform case: intensity remains constant up to high magnetic latitude along the magnetic field line.

and pitch angle dispersionless signatures. Tracing back to the magnetic equator, the flux of the resonant ions at the pitch angle of 90° has 90° phase difference with the electric field.

Observations and qualitative analyses in this case study indicate that the ULF wave-associated electric field most likely peaks near the magnetic equator. In the future study, statistical study and test particle simulations will be further used to explore the relationship between drift-bounce ions and different harmonic mode ULF waves.

5. Conclusion

When traveling inbound toward the inner magnetosphere from south to north near 1600 MLT on 3 June 2003, Cluster C1 observed simultaneous interaction of oxygen ions (10.5–35.1 keV) and protons (0.3–12.3 keV) with Pc5 ULF waves. The objective of this paper is to show the different behaviors of oxygen ions and protons which interact with the fundamental poloidal-mode ULF waves and further provide an approach to diagnose the morphology of the electric field as a function of latitude using the resonant ions signals. The observation and results are summarized as follows:

1. Observed Pc5 ULF waves are identified as fundamental-mode oscillations according to (1) drift resonance with energetic electrons, (2) drift-bounce resonance ($N = 2$) with ions, (3) phase relationship between B_r and E_a, and (4) modeling calculation.
2. Both oxygen ions and protons show the periodic energy dispersion and pitch angle dispersion signatures that satisfy the drift-bounce resonance condition of $N = 2$. For both types of ions, ULF waves with frequencies in the wave bandwidth(defined by the wave power dropping to half its maximum strength) play the dominant role in their acceleration/deceleration.
3. Oxygen ions and protons exhibit different behavior while simultaneously interacting with ULF waves, including (1) the resonant energy of oxygen ions is higher than that of protons due to mass difference; (2) the PSD of oxygen ions show relative variations (3.6–6.3) that are much larger than that of protons (<0.4), which indicates a more efficient energy exchange between oxygen ions and ULF waves; (3) the PSD spectra show that oxygen ions are accelerated, while protons are decelerated, which depend on the radial gradient of their PSD; and (4) the PADs of the oxygen ions and protons show negative slope and bidirectional field-aligned features, respectively, which is related to the preexisting state of ion PADs before the

interaction with ULF waves. These findings suggest that to further study the different behaviors of different ion species interacting with ULF waves could promote the understanding of the roles of ULF waves in the dynamics of ring current during storm times.

4. After tracing back to the magnetic equator, the peaks of both oxygen ion fluxes and proton fluxes at each energy and each pitch angle are all collocated with the westward accelerating electric field of poloidal-mode ULF waves. In this study, observations and qualitative analyses of different electric field morphologies support that the electric field intensity peaks near the magnetic equator.

Acknowledgments
This work was supported by the National Natural Science Foundation of China (41421003) and Major Project of Chinese National Programs for Fundamental Research and Development (2012CB825603). R. Rankin acknowledges the financial support of NSERC and the Canadian Space Agency. We thank the Cluster FGM, EFW, and CIS science teams for the data in this study. The Cluster data for this paper are available at the Cluster Science Archive. We also acknowledge Geoff Reeves (reeves@lanl.gov) for LANL data and NASA CDAWeb for WIND and OMNI data.

References

Balogh, A., et al. (1997), The Cluster magnetic field investigation, *Space Sci. Rev.*, *79*, 65–91.
Chaston, C., J. Bonnell, J. Wygant, C. Kletzing, G. Reeves, A. Gerrard, L. Lanzerotti, and C. Smith (2015), Extreme ionospheric ion energization and electron heating in Alfvén waves in the storm time inner magnetosphere, *Geophys. Res. Lett.*, *42*, 10,531–10,540, doi:10.1002/2015GL066674.
Chen, L., and A. Hasegawa (1974), A theory of long-period magnetic pulsations II. Impulse excitation of surface eigenmode, *J. Geophys. Res.*, *79*(7), 1033–1037.
Chen, L., and A. Hasegawa (1991), Kinetic theory of geomagnetic pulsations: 1. Internal excitations by energetic particles, *J. Geophys. Res.*, *96*(A2), 1503–1512.
Cheng, C., and Q. Qian (1994), Theory of ballooning-mirror instabilities for anisotropic pressure plasmas in the magnetosphere, *J. Geophys. Res.*, *99*(A6), 11,193–11,209.
Claudepierre, S., et al. (2013), Van allen probes observation of localized drift resonance between poloidal mode ultra-low frequency waves and 60 kev electrons, *Geophys. Res. Lett.*, *40*, 4491–4497, doi:10.1002/grl.50901.
Cummings, W., R. O'sullivan, and P. Coleman (1969), Standing Alfvén waves in the magnetosphere, *J. Geophys. Res.*, *74*(3), 778–793.
Daglis, I., W. Baumjohann, J. Gleiss, S. Orsini, E. Sarris, M. Scholer, B. Tsurutani, and D. Vassiliadis (1999), Recent advances, open questions and future directions in solar-terrestrial research, *Phys. Chem. Earth Part C*, *24*(1), 5–28.
Dai, L., et al. (2013), Excitation of poloidal standing Alfvén waves through drift resonance wave-particle interaction, *Geophys. Res. Lett.*, *40*, 4127–4132, doi:10.1002/grl.50800.
Degeling, A., L. Ozeke, R. Rankin, I. Mann, and K. Kabin (2008), Drift resonant generation of peaked relativistic electron distributions by Pc5 ULF waves, *J. Geophys. Res.*, *113*, A02208, doi:10.1029/2007JA012411.
Degeling, A., R. Rankin, K. Kabin, I. Rae, and F. Fenrich (2010), Modeling ULF waves in a compressed dipole magnetic field, *J. Geophys. Res.*, *115*, A10212, doi:10.1029/2010JA015410.
Elkington, S. R., M. K. Hudson, and A. A. Chan (1999), Acceleration of relativistic electrons via drift-resonant interaction with toroidal-mode Pc-5 ULF oscillations, *Geophys. Res. Lett.*, *26*(21), 3273–3276.
Escoubet, C. P., M. Fehringer, and M. Goldstein (2001), Introduction the Cluster mission, *Ann. Geophys.*, *19*(10/12), 1197–1200.
Foster, J., J. Wygant, M. Hudson, A. Boyd, D. Baker, P. Erickson, and H. E. Spence (2015), Shock-induced prompt relativistic electron acceleration in the inner magnetosphere, *J. Geophys. Res. Space Physics*, *120*, 1661–1674, doi:10.1002/2014JA020642.
Fu, S., B. Wilken, Q. Zong, and Z. Pu (2001), Ion composition variations in the inner magnetosphere: Individual and collective storm effects in 1991, *J. Geophys. Res.*, *106*(A12), 29,683–29,704.
Fujita, S., K.-H. Glassmeier, and K. Kamide (1996), MHD waves generated by the kelvin-helmholtz instability in a nonuniform magnetosphere, *J. Geophys. Res.*, *101*(A12), 27,317–27,325.
Fujita, S., T. Tanaka, and T. Motoba (2011), Long-period ULF waves driven by periodic solar wind disturbances, in *The Dynamic Magnetosphere*, pp. 39–45, Springer, Netherlands.
Hamlin, D. A., R. Karplus, R. C. Vik, and K. M. Watson (1961), Mirror and azimuthal drift frequencies for geomagnetically trapped particles, *J. Geophys. Res.*, *66*(1), 1–4, doi:10.1029/JZ066i001p00001.
Hughes, W. J. (1994), Magnetospheric, ULF waves: A tutorial with a historical perspective, in *Solar Wind Sources of Magnetospheric Ultra-Low-Frequency Waves*, pp. 1–11, AGU, Washington, D. C.
Jacobs, J., Y. Kato, S. Matsushita, and V. Troitskaya (1964), Classification of geomagnetic micropulsations, *J. Geophys. Res.*, *69*(1), 180–181.
Kepko, L., and H. E. Spence (2003), Observations of discrete, global magnetospheric oscillations directly driven by solar wind density variations, *J. Geophys. Res.*, *108*(A6), 1257, doi:10.1029/2002JA009676.
Kepko, L., H. E. Spence, and H. Singer (2002), ULF waves in the solar wind as direct drivers of magnetospheric pulsations, *Geophys. Res. Lett.*, *29*(8), 1197, doi:10.1029/2001GL014405.
Laakso, H., et al. (2010), Cluster active archive: Overview, in *The Cluster Active Archive*, pp. 3–37, Springer, Netherlands.
Lavraud, B., C. Foullon, C. J. Farrugia, and J. P. Eastwood (2011), The magnetopause, its boundary layers and pathways to the magnetotail, in *The Dynamic Magnetosphere*, pp. 3–28, Springer, Netherlands.
Liu, W., et al. (2013), Poloidal ULF wave observed in the plasmasphere boundary layer, *J. Geophys. Res. Space Physics*, *118*, 4298–4307, doi:10.1002/jgra.50427.
Malaspina, D. M., S. G. Claudepierre, K. Takahashi, A. N. Jaynes, S. R. Elkington, R. E. Ergun, J. R. Wygant, G. D. Reeves, and C. A. Kletzing (2015), Kinetic Alfvén waves and particle response associated with a shock-induced, global ULF perturbation of the terrestrial magnetosphere, *Geophys. Res. Lett.*, *42*(21), 9203–9212, doi:10.1002/2015GL065935.
Mathie, R., and I. Mann (2000), A correlation between extended intervals of ULF wave power and storm-time geosynchronous relativistic electron flux enhancements, *Geophys. Res. Lett.*, *27*(20), 3261–3264.
Mathie, R., and I. Mann (2001), On the solar wind control of Pc5 ULF pulsation power at mid-latitudes: Implications for MeV electron acceleration in the outer radiation belt, *J. Geophys. Res.*, *106*(A12), 29,783–29,796.
McPherron, R. L. (2005), Magnetic pulsations: Their sources and relation to solar wind and geomagnetic activity, *Surv. Geophys.*, *26*(5), 545–592.
Ogilvie, K., et al. (1995), SWE, a comprehensive plasma instrument for the Wind spacecraft, *Space Sci. Rev.*, *71*(1–4), 55–77.
Pedersen, A., et al. (2008), Electron density estimations derived from spacecraft potential measurements on Cluster in tenuous plasma regions, *J. Geophys. Res.*, *113*, A07S33, doi:10.1029/2007JA012636.
Rae, I., et al. (2005), Evolution and characteristics of global Pc5 ULF waves during a high solar wind speed interval, *J. Geophys. Res.*, *110*, A12211, doi:10.1029/2005JA011007.

Rème, H., et al. (2001), First multispacecraft ion measurements in and near the Earth's magnetosphere with the identical Cluster Ion Spectrometry (CIS) experiment, *Ann. Geophys.*, *19*, 1303–1354.
Ren, J., Q. Zong, Y. Wang, and X. Zhou (2015), The interaction between ULF waves and thermal plasma ions at the plasmaspheric boundary layer during substorm activity, *J. Geophys. Res. Space Physics*, *120*(2), 1133–1143, doi:10.1002/2014JA020766.
Rostoker, G., S. Skone, and D. N. Baker (1998), On the origin of relativistic electrons in the magnetosphere associated with some geomagnetic storms, *Geophys. Res. Lett.*, *25*(19), 3701–3704.
Singer, H. J., W. J. Hughes, and C. T. Russell (1982), Standing hydromagnetic waves observed by ISEE 1 and 2: Radial extent and harmonic, *J. Geophys. Res.*, *87*, 3519–3529.
Southwood, D. (1976), A general approach to low-frequency instability in the ring current plasma, *J. Geophys. Res.*, *81*(19), 3340–3348.
Southwood, D., J. Dungey, and R. Etherington (1969), Bounce resonant interaction between pulsations and trapped particles, *Planet. Space Sci.*, *17*(3), 349–361.
Southwood, D. J., and M. G. Kivelson (1981), Charged particle behavior in low-frequency geomagnetic pulsations. I: Transverse waves, *J. Geophys. Res.*, *86*, 5643–5655.
Southwood, D. J., and M. G. Kivelson (1982), Charged particle behavior in low-frequency geomagnetic pulsations. Ii—Graphical approach, *J. Geophys. Res.*, *87*, 1707–1710.
Takahashi, K., R. W. McEntire, A. T. Y. Lui, and T. A. Potemra (1990), Ion flux oscillations associated with a radially polarized transverse Pc 5 magnetic pulsation, *J. Geophys. Res.*, *95*, 3717–3731.
Takahashi, K., P. J. Chi, R. E. Denton, and R. L. Lysak (2006), A review of ULF interactions with radiation belt electrons, in *Magnetospheric ULF Waves: Synthesis and New Directions*, vol. 169, AGU, 177–193. Washington, D. C.
Takahashi, K., K.-H. Glassmeier, V. Angelopoulos, J. Bonnell, Y. Nishimura, H. J. Singer, and C. T. Russell (2011), Multisatellite observations of a giant pulsation event, *J. Geophys. Res.*, *116*, A11223, doi:10.1029/2011JA016955.
Tsyganenko, N. (1989), A magnetospheric magnetic field model with a warped tail current sheet, *Planet. Space Sci.*, *37*(1), 5–20.
Wilken, B., et al. (1997), RAPID—The imaging energetic particle spectrometer on cluster, *Space Sci. Rev.*, *79*(1–2), 399–473.
Williams, D. (1981), Ring current composition and sources: An update, *Planet. Space Sci.*, *29*(11), 1195–1203.
Williams, D (1983), The Earth's ring current: Causes, generation, and decay, *Space Sci. Rev.*, *34*(3), 223–234.
Williams, D. (1985), Dynamics of the Earth's ring current: Theory and observation, *Space Sci. Rev.*, *42*(3–4), 375–396.
Yang, B., Q. Zong, Y. F. Wang, S. Y. Fu, P. Song, H. S. Fu, A. Korth, T. Tian, and H. Reme (2010), Cluster observations of simultaneous resonant interactions of ULF waves with energetic electrons and thermal ion species in the inner magnetosphere, *J. Geophys. Res.*, *115*, A02214, doi:10.1029/2009JA014542.
Yang, B., Q.-G. Zong, S. Y. Fu, X. Li, A. Korth, H. S. Fu, C. Yue, and H. Reme (2011a), The role of ULF waves interacting with oxygen ions at the outer ring current during storm times, *J. Geophys. Res.*, *116*, A01203, doi:10.1029/2010JA015683.
Yang, B., et al. (2011b), Pitch angle evolutions of oxygen ions driven by storm time ULF poloidal standing waves, *J. Geophys. Res.*, *116*, A03207, doi:10.1029/2010JA016047.
Zhou, X.-Z., Z.-H. Wang, Q.-G. Zong, R. Rankin, M. G. Kivelson, X.-R. Chen, J. B. Blake, J. R. Wygant, and C. A. Kletzing (2016), Charged particle behavior in the growth and damping stages of ultralow frequency waves: Theory and van allen probes observations, *J. Geophys. Res. Space Physics*, *121*, 3254–3263, doi:10.1002/2016JA022447.
Zhou, X.-Z., et al. (2015), Imprints of impulse-excited hydromagnetic waves on electrons in the van allen radiation belts, *Geophys. Res. Lett.*, *42*, 6199–6204, doi:10.1002/2015GL064988.
Zong, Q., B. Wilken, S. Fu, T. Fritz, Z. Pu, N. Hasebe, and D. Williams (2001), Ring current oxygen ions in the magnetosheath caused by magnetic storm, *J. Geophys. Res*, *106*, 25–541.
Zong, Q., Y. Wang, B. Yang, S. Fu, Z. Pu, L. Xie, and T. A. Fritz (2008), Recent progress on ULF wave and its interactions with energetic particles in the inner magnetosphere, *Sci. China Ser. E*, *51*(10), 1620–1625.
Zong, Q.-G., et al. (2007), Ultralow frequency modulation of energetic particles in the dayside magnetosphere, *Geophys. Res. Lett.*, *34*, L12105, doi:10.1029/2007GL029915.
Zong, Q.-G., et al. (2009), Energetic electrons response to ULF waves induced by interplanetary shocks in the outer radiation belt, *J. Geophys. Res.*, *114*, A10204, doi:10.1029/2009JA014393.
Zong, Q.-G., Y. F. Wang, H. Zhang, S. Y. Fu, H. Zhang, C. R. Wang, C. J. Yuan, and I. Vogiatzis (2012), Fast acceleration of inner magnetospheric hydrogen and oxygen ions by shock induced ULF waves, *J. Geophys. Res.*, *117*, A11206, doi:10.1029/2012JA018024.